metals

MDPI

Communication

High Thermal Stability of a Colony and Basket-Weave Mixed Microstructure in Selective-Laser-Melted Ti-6Al-4V AlloyInduced by Electropulsing

Lai Wei [1], Xiaofeng Xu [1,2,*], Yang Zhao [2,3], Xudong Yan [1], Yachong Zhou [1], Zhicheng Wu [1] and Yongqiang Yu [1]

[1] Key Laboratory of Automobile Materials, Ministry of Education and Department of Materials Science and Engineering, Jilin University, Changchun 130022, China
[2] Weihai Institute for Bionics, Jilin University, Weihai 130022, China
[3] Key Laboratory of Bionic Engineering, Ministry of Education, Jilin University, Changchun 130022, China
* Correspondence: xuxiaofeng@jlu.edu.cn

Abstract: A colony and basket-weave mixed microstructure in the selective-laser-melted (SLM) Ti-6Al-4V alloy was introduced by electropulsing, which showed high thermal stability. The mechanism was investigated by electron backscatter diffraction (EBSD) and X-ray diffraction (XRD) analysis. It was found that the low content of the β-phase favored the inhibition of microstructure coarsening. The increasing β-phases during the stabilization annealing (700 °C/16 h) rendered the growth of α-lath and -colony. Moreover, the stabilization-annealed colony and basket-weave mixed microstructure still kept the high strength–ductility synergy.

Keywords: selective-laser-melted Ti-6Al-4V alloy; electropulsing; thermal stability; β-phase; strength–ductility synergy

check for updates

Citation: Wei, L.; Xu, X.; Zhao, Y.; Yan, X.; Zhou, Y.; Wu, Z.; Yu, Y. High Thermal Stability of a Colony and Basket-Weave Mixed Microstructure in Selective-Laser-Melted Ti-6Al-4V AlloyInduced by Electropulsing. *Metals* **2023**, *13*, 538. https://doi.org/10.3390/met13030538

Academic Editor: Reza Ghomashchi

Received: 11 February 2023
Revised: 3 March 2023
Accepted: 4 March 2023
Published: 7 March 2023

Copyright: © 2023 by the authors. Licensee MDPI, Basel, Switzerland. This article is an open access article distributed under the terms and conditions of the Creative Commons Attribution (CC BY) license (https://creativecommons.org/licenses/by/4.0/).

1. Introduction

Selective-laser-melting (SLM) technology to produce complex metallic components has exhibited its effectiveness in manufacturing. The Ti-6Al-4V alloy, the workhorse of the titanium industry, has a high specific strength, excellent corrosion resistance, and outstanding biocompatibility [1,2]. It, by far, has been one of the most used and studied titanium alloys for SLM [3]. Typically, the fast cooling rate (around 103–108 K/s) would induce a martensite microstructure in the SLM-fabricated Ti-6Al-4V alloy and result in reduced ductility [4,5]. This martensite microstructure contains a high density of crystallographic defects, e.g., dislocations, twin boundaries, and stacking faults [6], and has inhibited the widespread application of the as-built Ti-6Al-4V alloy. Therefore, post-treatment to optimize the microstructure is required. Due to the near-net shape characteristic, the most common approaches contain hot isostatic pressing (HIP) and post-heat treatments. Yu et al. [7] applied a HIP process to tailor the as-built microstructure of the SLM-fabricated Ti-6Al-4V alloy and significantly improve the ductility. However, the HIP is a high-cost process, and the AM (additive manufacturing) component with low porosity is commonly heat treated. Sub-transus heat treatments followed by water quenching that could produce an α + α′ microstructure have been used to optimize the electron beam melting (EBM) or SLM Ti-6Al-4V alloy [8–10]. This microstructure exhibited a composite work-hardening behavior and induced high room-temperature strength–ductility synergy in the AM Ti-6Al-4V alloy. Nevertheless, α′ is not a thermally stable phase and will decompose when the temperature exceeds 400 °C [6]. There is a requirement for microstructure near thermodynamic equilibrium when the titanium component is applied to serve under elevated-temperature environments. Kim et al. [11] annealed the SLM-fabricated Ti-6Al-4V alloy at 1040 °C for 1 h to achieve a Widmanstätten structure, and the annealed microstructure showed a superior creep resistance. However, this Widmanstätten structure commonly shows a low elongation.

Electropulsing treatment combining thermal and athermal effects can promote dislocation mobility and shows great potential for optimizing the microstructure of metals [12]. Several researchers have used electropulsing to tailor the microstructure of SLM-fabricated Ti-6Al-4V alloys, and the modified microstructure showed enhanced mechanical properties [13–15]. However, rare studies have focused on the thermal stability of the microstructure after electropulsing optimization. In this study, we found that electropulsing could induce a colony and basket-weave mixed microstructure in the SLM-fabricated Ti-6Al-4V alloy and showed superior mechanical properties. Since this mixed microstructure is obtained by air cooling, it is expected that it has excellent thermal stability. Therefore, this study aims to characterize the thermal stability of the colony and basket-weave mixed microstructure by evaluating the microstructure and mechanical-property changes after a stabilization-annealing treatment. As for the fundamentals that generate this mixed microstructure, we discuss them separately. To investigate the thermal stability of the mixed microstructure better, a super-transus heat-treated sample was also characterized as a contrast. It is hoped that the systematic characterization will verify that electropulsing can act as an effective method to achieve high-thermal-stability microstructure and provide a glimpse into the microstructural parameters which play vital roles in thermal stability.

2. Materials and Methods

Cubic specimens with dimensions of 50 × 50 × 10 mm^3 were produced on an SLM system (BLT S210, Xi'an, China) using Ti-6Al-4V alloy powder (Figure 1a). Commercial spherical Ti-6Al-4V powder with a particle size distribution of 15–53 μm was used. A laser power setting of 210 W, a scanning speed of 1200 mm/s, a layer thickness of 30 μm, and an incubation distance of 80 μm were used to produce the specimens. A zigzag continuous-laser-scanning strategy was used, and the scanning pattern between each layer was rotated by 67°. Cubic specimens were machined into 50.0 × 10.0 × 2.5 mm^3 by wire-electrode cutting along the x-axis for the subsequent treatment. The as-built (labeled as AB), super-transus, heat-treated (labeled as HT; at 1020 °C for 5 min, followed by air cooling), and electropulsing-processed (labeled as EPT; at 45.5 A/mm^2 and 50 Hz for 400 ms, followed by air cooling) samples were stabilization annealed at 700 °C for 16 h, followed by air cooling, and designated as ABA, HTA, and EPTA, respectively. The annealing treatment was conducted on a tube furnace with the protection of argon. The specimens for microstructure analysis were prepared by sandpaper grinding, SiO_2 suspension polishing, and etching by Kroll's solution (using 13 mL of HF, 26 mL of HNO_3, and 100 mL of H_2O). Scanning electron microscope (SEM; Tescan Vega3, Tescan Company, Brno, Czech Republic), electron backscatter diffraction (EBSD; Oxford Symmetry; with a step size of 0.2–0.8 μm), transmission electron microscope (TEM; JEM-2100), Nippon Electronics Co., Japan, and X-ray diffraction (XRD; with D/max 2500pc, Cu Kα, and 1°/min) were used to examine the microstructures. Tensile specimens had gauge dimensions of 10 mm × 2.2 mm × 2.2 mm (Figure 1b). The dimension of the tensile specimens was determined according to GB6397-86. Tensile tests were conducted on an MTS-810 system at room temperature, and the strain rate was at a speed of 10^{-3} s^{-1} (0.6 mm/min). The tensile direction was parallel to the y-axis. At least three samples were tested for each condition, and the dimensions of each sample were precisely measured in our studies.

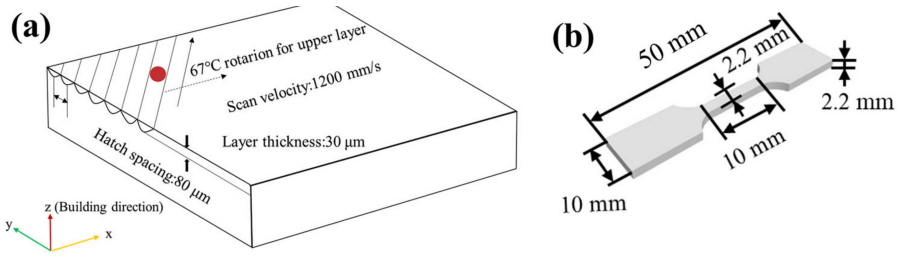


Figure 1. Schematic diagrams of (**a**) cubic specimen and (**b**) tensile specimen.

3. Results and Discussion

Backscattered SEM micrographs of the samples before and after the stabilization annealing are exhibited in Figure 2. After the annealing, the martensite structure of AB was fully transformed into basket-weave α-structure with the width increased by 67% from ~0.73 μm to ~1.22 μm, as shown in Figure 2a,d. Due to the decomposition of α′, there were much more β-phases (white color) in the ABA (Figure 2d). The HT and HTA exhibited colony microstructures with alternate layers of α-lath (gray) and β-film (white), as shown in Figure 2b,e. Compared to HT, α-lath width in HTA shows a 25% increase from ~1.02 μm to ~1.27 μm, and more β-phase particles and thinner β-films can be observed in the HTA. The EPT and EPTA show colony and basket-weave mixed microstructures, and the α-plate width in the latter (~1.1 μm) is 16% larger than the former (~0.94 μm), as shown in Figure 2c,f. It should be noted that only faint white films can be seen in the EPT, which possibly was caused by the competition nucleation and growth of the α-variants at prior-β-grain boundaries and intragranular areas, leaving little time for the aggregation of V atoms and coarsening of β-film. The stabilization annealing accelerated the aggregation of V and resulted in more β-phase particles with a brighter white color (Figure 2f). The TEM micrograph of AB (Figure 2g) shows that there were many dislocations existing in the martensitic laths, and this is a typical characteristic of the SLM as-built microstructure [6]. The widths of the β-films ranged from 25 nm to 50 nm (Figure 2h); therefore, they are almost invisible in the SEM micrograph. More importantly, as displayed in Figure 2i, some nano stacking faults (SFs) could be found within the α-lath, which is demonstrated by the streaking of diffraction spots in the corresponding SAED [16]. The nano SFs are speculated to come from the decomposition of the dislocations produced by thermal stress.

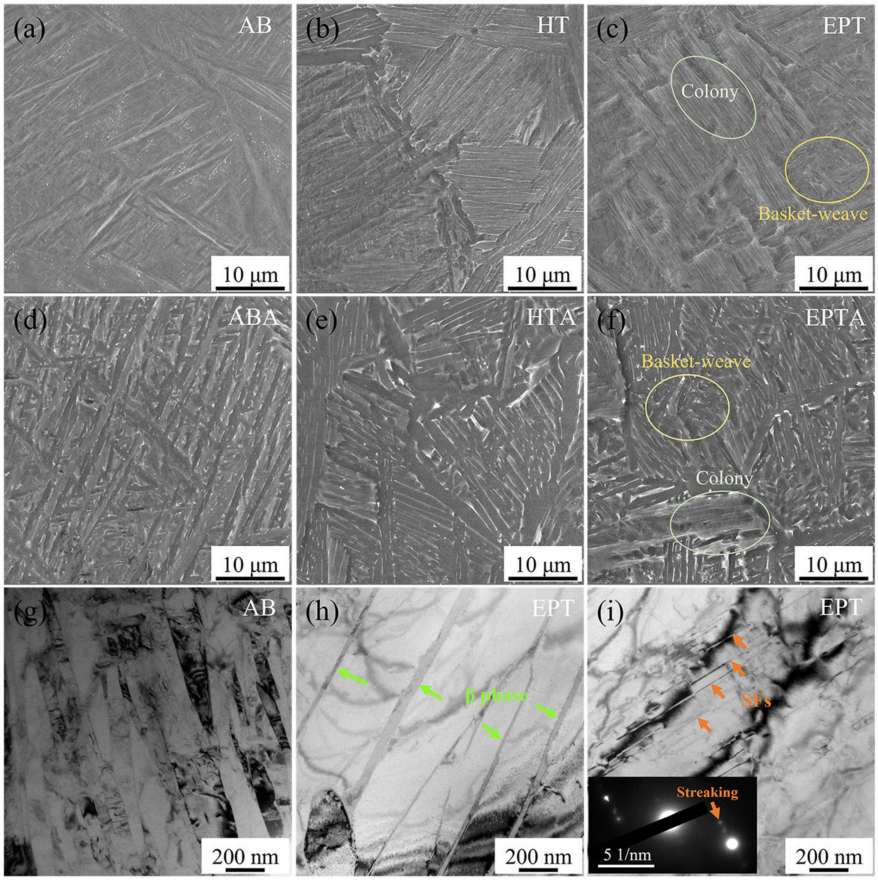


Figure 2. Backscattered SEM micrographs of samples before and after the stabilization annealing: (**a**) AB, (**b**) HT, (**c**) EPT, (**d**) ABA, (**e**) HTA, (**f**) EPTA. TEM micrographs of such samples: (**g**) AB, (**h**,**i**) EPT.

In Figure 3, EBSD inverse-pole-figure (IPF) maps and corresponding kernel-average-misorientation (KAM) maps of the specimens are presented. The AB was characterized by acicular α'-microstructure (Figure 3a). The HT sample showed a typical colony microstructure [17], and the average colony size was around 13.1 µm (Figure 3b). The EPT sample exhibited a colony and basket-weave microstructure, and the average colony size was around 7.1 µm (Figure 3c). The stabilization annealing made the microstructures coarsen at different degrees, which is inconsistent with SEM observations in Figure 3. The colony size increased by 24%, to around 16.3 µm, in HTA (Figure 3h) and increased by 18%, to around 8.4 µm, in EPTA (Figure 3i). KAM maps indicate that the dislocation contents in the samples were significantly reduced by the stabilization annealing. The average KAM value decreased from 1.3° in AB to 0.8° in ABA (Figure 3d,j). Moreover, the KAM values decreased from 0.83° (HT) and 1.16° (EPT) to 0.68° (HTA, EPTA), as displayed in Figure 3e,f,k,l.

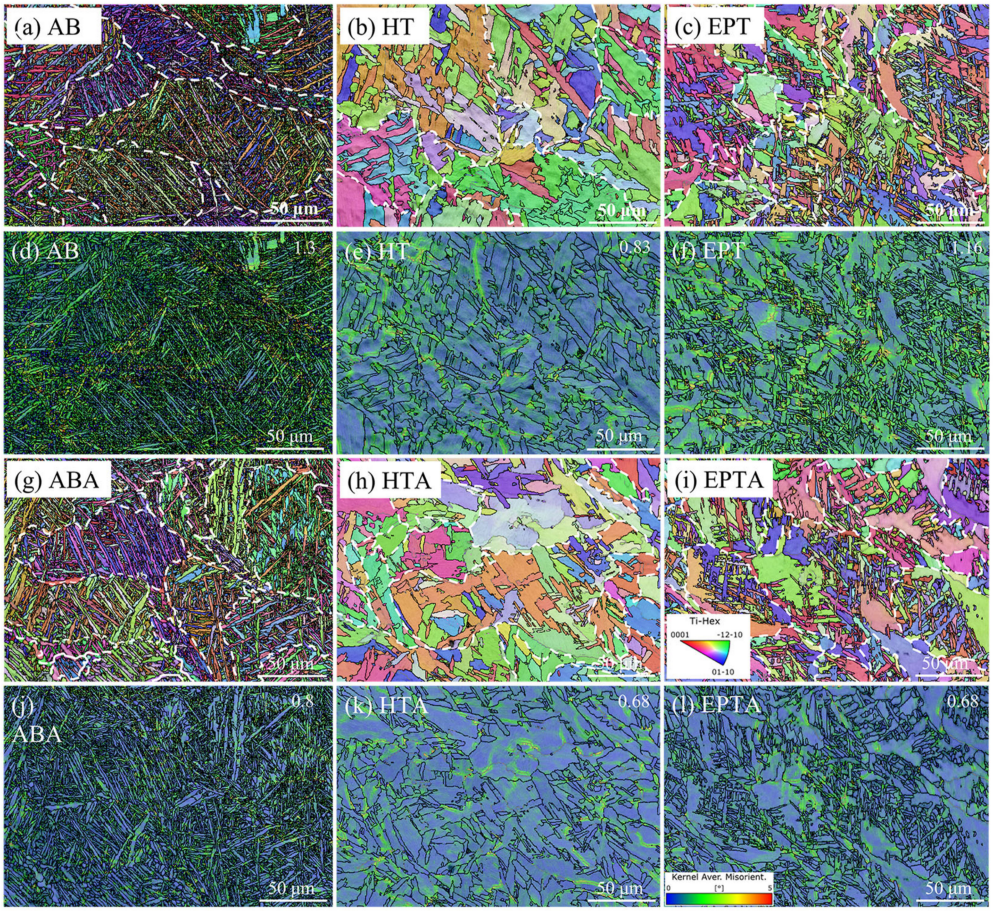


Figure 3. IPF maps and KAM maps of the samples. IPF maps: (**a**) AB, (**b**) HT, (**c**) EPT, (**g**) ABA, (**h**) HTA, (**i**) EPTA; KAM maps: (**d**) AB, (**e**) HT, (**f**) EPT, (**j**) ABA, (**k**) HTA, (**l**) EPTA.

Distributions of the β-phases in the typical samples are characterized by the phase maps obtained from the EBSD data, as shown in Figure 4a–d. The stabilization-annealing treatments of the HT and EPT result in a larger size and higher amounts of β-phase particles in the HTA and EPTA, respectively. Moreover, the β-phase particle size of HTA is larger than the EPTA (Figure 4c,d). The limited detecting surface and the step size may affect the accuracy of the β-phase content obtained from the EBSD. The XRD results provide additional analysis on the β-phase content that complements the EBSD phase-map observations. As shown in Figure 4e, the intensity of the β (110)-peak of the EPT sample is significantly lower than the HT sample (α (01-10)-peaks with the same intensities). The intensity ratio of β (110)/α (01-10) for HT is consistent with the value for a super-transus,

annealed, and air-cooled Ti-6Al-4V alloy [18], which indicates a similar β-content. After long-time annealing at 700 °C, the β (110)-peak intensity shows decreased value in the HTA (compared to the HT) but shows an increasing value in the EPTA (compared to the EPT). The reference-intensity-ratio (RIR) method [19] was employed to determine the β-contents in HT, EPT, HTA, and EPTA samples. The fraction ratio of β can be determined by the following equation:

$$X_\beta = \frac{I_\beta^{max}/RIR_\beta}{\frac{I_\beta^{max}}{RIR_\beta} + \frac{I_\alpha^{max}}{RIR_\alpha}} \quad (1)$$

where X_β is the volume fraction of the β-phase, I $I^{max}$is the intensity of the highest diffraction peak of the phase, and RIR is the reference intensity ratio of the phase. RIR_β is 9.6, and the RIRα is 6.4. The β-contents of the HT, EPT, HTA, and EPTA were calculated to be 9.6 wt%, 4.3 wt%, 5.6 wt%, and 5.6 wt%, respectively, as shown in Figure 4f. The results from the EBSD and XRD methods show considerable differences, which are mainly attributed to the step size of the EBSD not being small enough (0.2 μm). The width of the β-film was even smaller than 50 nm (Figure 2h). Therefore, many β-films could not be detected by the EBSD, and the obtained β-content values were much smaller than the values from the XRD.

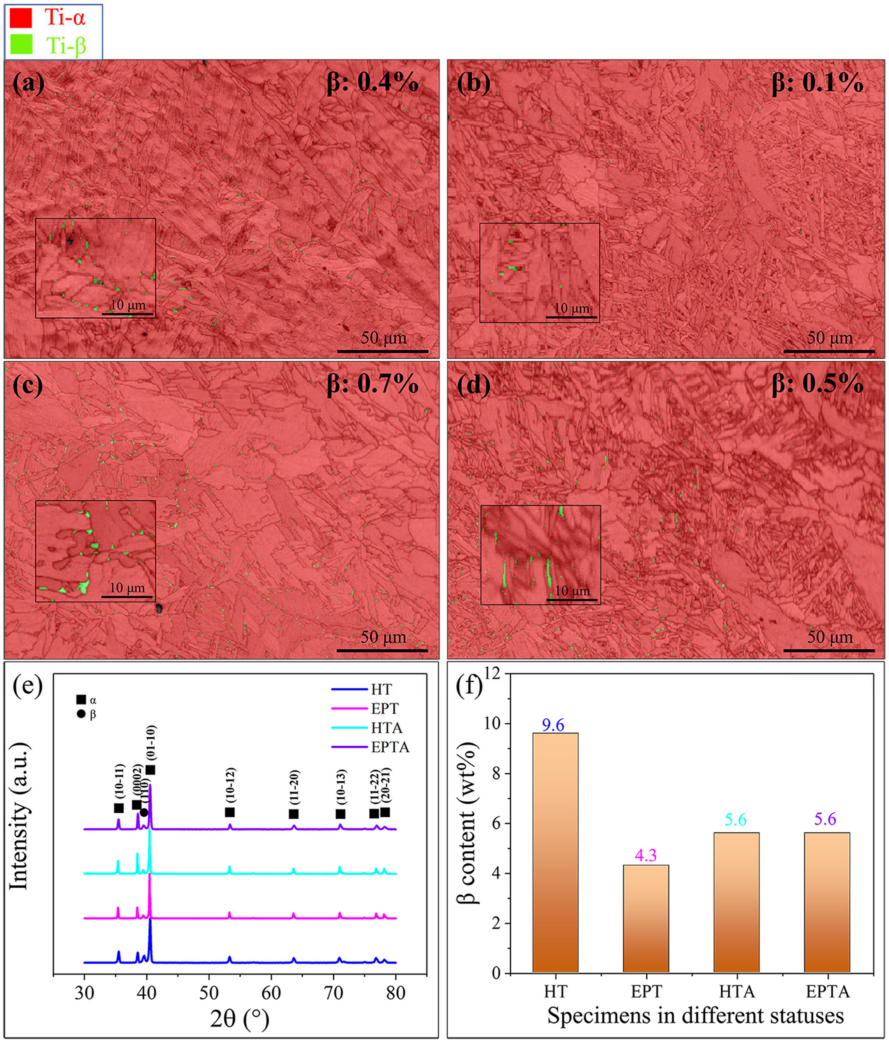


Figure 4. Phase maps: (**a**) HT, (**b**) EPT, (**c**) HTA, (**d**) EPTA; (**e**) XRD patterns and (**f**) β-contents calculated by RIR method.

Thermal stability can be affected by several factors, such as dislocation content, grain orientation, elemental partitioning [16], and the β-phase content [20]. High-density dislocations will provide a driving force for the growth of the α'- and α-lathes because they support the rapid diffusion of alloying elements [21]. Similar grain orientations of the α-lath can minimize the interface energy and hinder the growth of α-lath [16]. Furthermore, the aggregation of V atoms at the α-boundaries will inhibit the α-lath growth [22], and higher β-phase content also can impede the coarsening of α-lath [20]. The as-built microstructure shows low thermal stability (with a 67% increase in lath width) due to the inherent metastability and high dislocation content of the α'-phase. In contrast, the HT and EPT exhibit much higher thermal stability due to the reduced dislocation density, more V atoms aggregating at the grain boundary, and similar orientations of α-lathes. It is important to note that the EPT sample possesses higher thermal stability than the HT sample (with an increase in α-lath width of 16% vs. 25%, respectively, and increase in α-colony size of 18% vs. 24%, respectively), in addition to the EPT possessing greater dislocation density, less V aggregation, and fewer similar-orientated α-laths than the HT. It indicates that the β-phase content plays an essential role in the thermal stability of the EPT sample. The HT shows a much higher β-content (9.6 wt%) than the EPT (4.3 wt%). After long-time annealing at 700 °C, the HTA and EPTA show the same β-contents, which indicates that the β-content of the Ti-6Al-4V alloy in the equilibrium state is around 5.6 wt%. When annealed at 700 °C, the decrease of β-content in the HT favors the growth of α-lath and α-colony. Nevertheless, the β-content of EPT increases and inhibits the growth of α-lath and α-colony.

Tensile engineering stress–strain, true stress–strain, work-hardening rate curves, and detailed tensile properties of the samples after stabilization annealing are presented in Figure 5a,b and Table 1. The yield strength (YS), ultimate tensile strength (UTS), and elongation (EL) of the ABA sample are (1002 ± 22) MPa, (1050 ± 9) MPa, and (10.7 ± 0.8) %, respectively. All tensile properties of the HTA sample are inferior to the ABA, and the YS, UTS, and EL are (949 ± 19) MPa, (1019 ± 17) MPa, and (10.3 ± 0.8) %, respectively. Compared to the ABA sample, the EPTA shows slightly lower YS (976 ± 1) MPa, similar UTS (1049 ± 5) MPa, and distinctly (~35.5%) higher EL at (14.5 ± 1.4) %. As a result, the EPTA shows the highest strength–ductility synergy. Figure 5c,d shows the changes in mechanical properties induced by stabilization-annealing treatment. The UTS and YS for AB decreased by ~258 MPa and ~160 MPa, respectively. The UTS values for HT and EPT kept almost stable, while the YS was slightly enhanced by ~34 MPa and ~51 MPa, respectively. The attribution of β-phase content on the YS of the Ti-6Al-4V alloy is small [23,24]. Nevertheless, the morphology of the β-phase significantly affects the local deformation mechanisms and mechanical properties of α + β Ti-6Al-4V alloys [25]. Consequently, because the decrease of dislocations and increase in grain size will reduce the YS, the enhancements of YS values in both HTA and EPTA are mainly attributed to the morphology change of the β-phase. As for the elongation, it increased by ~2% for AB, decreased by ~2% for HT, and decreased by ~1% for EPT. Fracture morphologies of the HTA and EPTA are shown in Figure 5e–h. The stabilization annealing does not significantly alter the fracture mechanism, and the HT and EPT show similar work-hardening rate curves and fracture morphologies. The EPTA still exhibits as high a post-uniform elongation as the EPT. The changes in tensile properties also indicate that the electropulsing induces a high thermal stability in the SLM Ti-6Al-4V alloy. Furthermore, the electropulsing process in this study requires less time (400 ms) than the HIP process [7], which means that the electropulsing process is not only more timesaving but also more energy efficient.

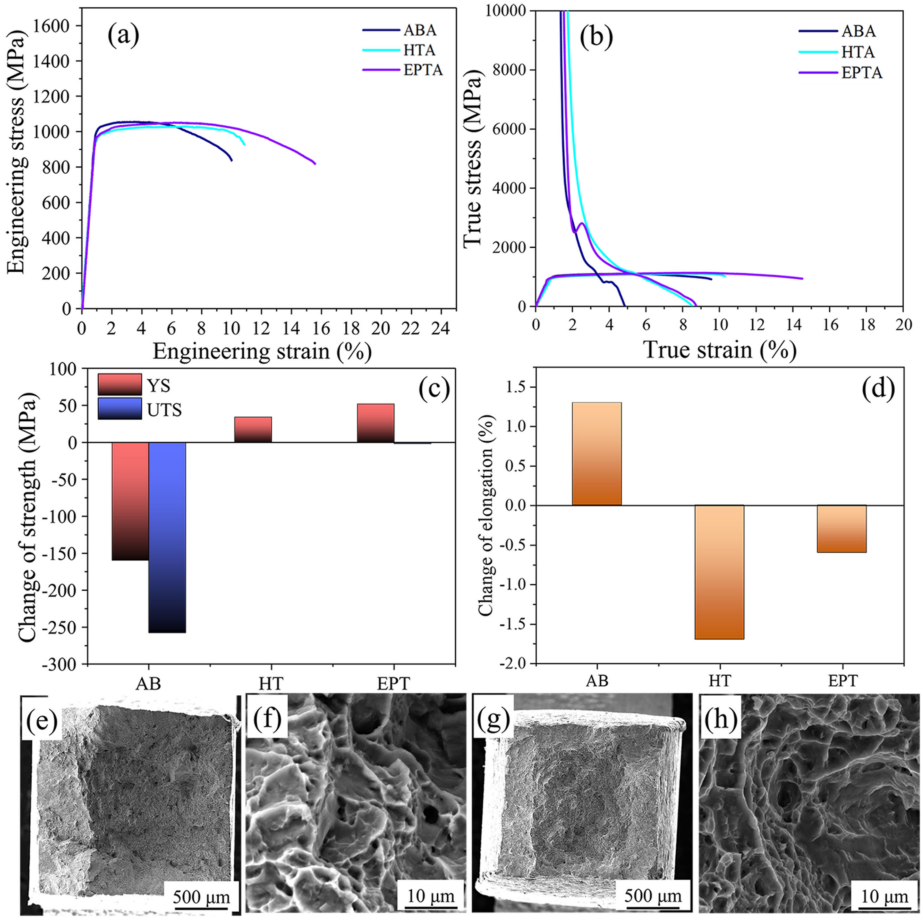


Figure 5. (**a**) Engineering stress–strain curves; (**b**) true stress–strain, work-hardening rate curves, and mechanical properties of the samples; (**c**,**d**) mechanical-property changes induced by the stabilization annealing; (**e**,**f**) fracture morphology of HTA; (**g**,**h**) fracture morphology of EPTA.

Table 1. Tensile properties of samples in different conditions.

	Yield Strength (YS) (0.2% Offset) [MPa]	Ultimate Tensile Stress (UTS) [MPa]	Elongation (EL) [%]
ABA	1002 ± 22	1050 ± 9	10.7 ± 0.8
HTA	949 ± 19	1019 ± 17	10.3 ± 0.8
EPTA	971 ± 1	1049 ± 5	14.5 ± 1.4

4. Conclusions

To summarize, stabilization-annealing treatments (700 °C/16 h) were carried out on the SLM Ti-6Al-4V alloys processed by furnace heat treatment (HT) and electropulsing (EPT) to evaluate their thermal stability. The colony and basket-weave microstructure of the EPT sample showed a lower degree of microstructure change than the HT sample, and the former showed 16% and 18% increases in α-lath width and α-colony size, respectively, while the latter exhibited 25% and 24% increases in α-lath width and α-colony size, respectively. The high thermal stability of the EPT sample was attributed to the low β-content, and the increasing β-phase during the stabilization annealing was attributed to the inhibition of the coarsening of microstructure. Moreover, the stabilization-annealed EPT sample kept the excellent strength–p (YS = (976 ± 1) MPa, UTS = (1049 ± 5) MPa, and EL = (14.5 ± 1.4)%). The present result showed a possibility for achieving thermally stable microstructures in SLM Ti-6Al-4V alloys by electropulsing, which possessed a higher strength–plasticity combination than the colony microstructure of furnace heat-treated alloys.

Author Contributions: Conceptualization, L.W. and X.X.; methodology, L.W., X.X., Y.Z. (Yang Zhao), X.Y., Y.Z. (Yachong Zhou), Z.W. and Y.Y.; writing—original draft preparation, L.W.; writing—review and editing, X.X.; supervision, X.X.; funding acquisition, X.X. All authors have read and agreed to the published version of the manuscript.

Funding: This work was supported by the National Key Research and Development Program of China (Nos. 2020YFB2008300, 2020YFB2008303, and 2020YFB2008304); the Provincial Natural Science Foundation of Shandong (Grant No. ZR202102220408); National Natural Science Foundation of China (Grant No. 51701080); and Talent Development—Excellent Young Talents Fund Project, China (Grant No. 20190103053JH).

Data Availability Statement: The data presented in this study are available on request from the corresponding author. The data are not publicly available due to technical and time limitations.

Conflicts of Interest: The authors declare no conflict of interest.

References

1. Lütjering, G. Influence of processing on microstructure and mechanical properties of (α + β) titanium alloys. *Mater. Sci. Eng. A* **1998**, *243*, 32–45. [CrossRef]
2. Rack, H.J.; Qazi, J.I. Titanium alloys for biomedical applications. *Mater. Sci. Eng. C.* **2006**, *26*, 1269–1277. [CrossRef]
3. Liu, S.; Shin, Y.C. Additive manufacturing of Ti6Al4V alloy: A review. *Mater. Des.* **2019**, *164*, 107552. [CrossRef]
4. Vilaro, T.; Colin, C.; Bartout, J.D. As-fabricated and heat-treated microstructures of the Ti-6Al-4V alloy processed by selective laser melting. *Metall. Mater. Trans. A Phys. Metall. Mater. Sci.* **2011**, *42*, 3190–3199. [CrossRef]
5. Kobryn, P.A.; Semiatin, S.L. The laser additive manufacture of Ti-6Al-4V. *Jom* **2001**, *53*, 40–42. [CrossRef]
6. Haubrich, J.; Gussone, J.; Barriobero-Vila, P.; Kürnsteiner, P.; Jägle, E.A.; Raabe, D.; Schell, N.; Requena, G. The role of lattice defects, element partitioning and intrinsic heat effects on the microstructure in selective laser melted Ti-6Al-4V. *Acta Mater.* **2019**, *167*, 136–148. [CrossRef]
7. Yu, H.; Li, F.; Wang, Z.; Zeng, X. Fatigue performances of selective laser melted Ti-6Al-4V alloy: Influence of surface finishing, hot isostatic pressing and heat treatments. *Int. J. Fatigue* **2019**, *120*, 175–183. [CrossRef]
8. Sofinowski, K.; Šmíd, M.; Kuběna, I.; Vivès, S.; Casati, N.; Godet, S.; Van Swygenhoven, H. In situ characterization of a high work hardening Ti-6Al-4V prepared by electron beam melting. *Acta Mater.* **2019**, *179*, 224–236. [CrossRef]
9. De Formanoir, C.; Brulard, A.; Vivès, S.; Martin, G.; Prima, F.; Michotte, S.; Rivière, E.; Dolimont, A.; Godet, S. A strategy to improve the work-hardening behavior of Ti–6Al–4V parts produced by additive manufacturing. *Mater. Res. Lett.* **2017**, *5*, 201–208. [CrossRef]
10. Zhang, D.; Wang, L.; Zhang, H.; Maldar, A.; Zhu, G.; Chen, W.; Park, J.S.; Wang, J.; Zeng, X. Effect of heat treatment on the tensile behavior of selective laser melted Ti-6Al-4V by in situ X-ray characterization. *Acta Mater.* **2020**, *189*, 93–104. [CrossRef]
11. Kim, Y.K.; Park, S.H.; Yu, J.H.; AlMangour, B.; Lee, K.A. Improvement in the high-temperature creep properties via heat treatment of Ti-6Al-4V alloy manufactured by selective laser melting. *Mater. Sci. Eng. A.* **2018**, *715*, 33–40. [CrossRef]
12. Liang, C.L.; Lin, K.L. The microstructure and property variations of metals induced by electric current treatment: A review. *Mater. Charact.* **2018**, *145*, 545–555. [CrossRef]
13. Waryoba, D.; Islam, Z.; Reutzel, T.; Haque, A. Electro-strengthening of the additively manufactured Ti–6Al–4V alloy. *Mater. Sci. Eng. A.* **2020**, *798*, 140062. [CrossRef]
14. Gao, J.B.; Ben, D.D.; Yang, H.J.; Meng, L.X.; Ji, H.B.; Lian, D.L.; Chen, J.L.; Yi, J.; Wang, L.; Li, P.; et al. Effects of electropulsing on the microstructure and microhardness of a selective laser melted Ti6Al4V alloy. *J. Alloys Compd.* **2021**, *875*, 160044. [CrossRef]
15. Wang, F.; Liu, Y.; Tong, Y.; Zhang, C.; Jiang, F.; Wang, J. Effect of electropulsing on anisotropy in strength of laser metal deposited Ti−6Al−4V alloy. *Trans. Nonferrous Met. Soc. China* **2022**, *32*, 2578–2586. [CrossRef]
16. Su, J.; Ji, X.; Liu, J.; Teng, J.; Jiang, F.; Fu, D.; Zhang, H. Revealing the decomposition mechanisms of dislocations and metastable α′ phase and their effects on mechanical properties in a Ti-6Al-4V alloy. *J. Mater. Sci. Technol.* **2022**, *107*, 136–148. [CrossRef]
17. Beladi, H.; Chao, Q.; Rohrer, G.S. Variant selection and intervariant crystallographic planes distribution in martensite in a Ti–6Al–4V alloy. *Acta Mater.* **2014**, *80*, 478–489. [CrossRef]
18. Gupta, A.; Khatirkar, R.K.; Kumar, A.; Parihar, M.S. Investigations on the effect of heating temperature and cooling rate on evolution of microstructure in an α + β titanium alloy. *J. Mater. Res.* **2018**, *33*, 946–957. [CrossRef]
19. Hubbard, C.R.; Snyder, R.L. RIR—Measurement and Use in Quantitative XRD. *Powder Diffr.* **1988**, *3*, 74–77. [CrossRef]
20. Margolin, H.; Izumi, O. *Titanium'80: Science and Technology*; TMS: Warrendale, PA, USA, 1980.
21. Semiatin, S.L.; Brown, T.M.; Goff, T.A.; Fagin, P.N.; Barker, D.R.; Turner, R.E.; Murry, J.M.; Miller, J.D.; Zhang, F. Diffusion Coefficients for Modeling the Heat Treatment of Ti-6Al-4V. *Metall. Mater. Trans. A* **2006**, *35*, 3015–3018. [CrossRef]
22. Meng, Y.; Villa, M.; Dahl, K.; Christiansen, T.L.; Somers, M.A.J. Synchrotron X-ray diffraction investigation of the effect of cryogenic treatment on the microstructure of Ti-6Al-4V. *Appl. Surf. Sci.* **2020**, *502*, 144087. [CrossRef]
23. Ghamarian, I.; Hayes, B.; Samimi, P.; Welk, B.A.; Fraser, H.L.; Collins, P.C. Developing a phenomenological equation to predict yield strength from composition and microstructure in β processed Ti-6Al-4V. *Mater. Sci. Eng. A* **2016**, *660*, 172–180. [CrossRef]

24. Ghamarian, I.; Samimi, P.; Dixit, V.; Collins, P.C. A Constitutive Equation Relating Composition and Microstructure to Properties in Ti-6Al-4V: As Derived Using a Novel Integrated Computational Approach. *Metall. Mater. Trans. A Phys. Metall. Mater. Sci.* **2015**, *46*, 5021–5037. [CrossRef]
25. Jun, T.S.; Sernicola, G.; Dunne, F.P.E.; Britton, T.B. Local deformation mechanisms of two-phase Ti alloy. *Mater. Sci. Eng. A.* **2016**, *649*, 39–47. [CrossRef]

Disclaimer/Publisher's Note: The statements, opinions and data contained in all publications are solely those of the individual author(s) and contributor(s) and not of MDPI and/or the editor(s). MDPI and/or the editor(s) disclaim responsibility for any injury to people or property resulting from any ideas, methods, instructions or products referred to in the content.